JGP Journal of General Physiology

ARTICLE

Contractile Function

Prediction and biological significance of small changes in binding of leiomodin to tropomyosin

Eduardo Sánchez Díaz[1], Brayan Osegueda[1*], Svetlana Minakhina[2*], Nickolas Starks[1*], Stefanie Novak[3], Dmitri Tolkatchev[1], Carol C. Gregorio[2,3], Alla S. Kostyukova[1], and Garry E. Smith Jr[1]

In cardiac muscle, regulation of actin polymerization at the thin filament pointed end is controlled by two structurally similar but functionally antagonistic proteins, leiomodin-2 and tropomodulin-1. Both proteins contain tropomyosin-binding site 1, which is essential for their recruitment to the pointed end. Using circular dichroism, we determined changes in melting temperatures (ΔT_m) for complexes of tropomyosin and leiomodin-2 fragments containing several hypomorphic mutations, which moderately affect binding to tropomyosin. We ran molecular dynamics simulations for the complexes and calculated standard Gibbs free energies of binding, which we found to strongly correlate with the ΔT_m. We found that the E34Q mutation in leiomodin-2 resulted in a decrease in the melting temperature of the complex of tropomyosin and leiomodin-2 fragments, indicating a decrease in the affinity of leiomodin-2 for tropomyosin. Although modest, this change in in vitro affinity made leiomodin-2 a weaker competitor for tropomyosin than tropomodulin-1 in cardiomyocytes. This mutation significantly reduced the ability of leiomodin-2 to displace tropomodulin-1 at thin filament pointed ends and affected the ability of leiomodin-2 to elongate thin filaments. Our results highlight the essential role of the tropomyosin-binding site in the dynamic equilibrium between tropomodulin-1 and leiomodin-2 at the pointed end of thin filaments. Our data also suggest the potential use of the correlation between ΔT_m and the modeled standard Gibbs free energies of binding to predict changes in the stability of complexes between tropomyosin and leiomodin or tropomodulin isoforms.

Introduction

Understanding the molecular mechanism of muscle function, particularly within the sarcomere structure, is pivotal for unraveling the complexities of muscle physiology. Important to this understanding is the interplay between various proteins, such as tropomyosin (Tpm) and proteins of the tropomodulin (Tmod) family, Tmod and leiomodin (Lmod), which govern the regulation of thin filament length in striated muscle sarcomeres (for reviews, see Fowler and Dominguez [2017]; Tolkatchev et al. [2022]). Sarcomeres are the fundamental units of muscle contraction, characterized by alternating overlapping thick and thin filaments (Henderson et al., 2017; Sweeney and Hammers, 2018, Szikora et al., 2022). The thick filament core is composed of myosin, while the thin filament core is composed of actin. The overlapping thick and thin filaments interact and slide to contract the sarcomere. Tpm, an actin-binding coiled-coil protein, occupies a central role in this regulation (Brown and Cohen, 2005). It binds to both sides of the thin filament polymerizing in a head-to-tail fashion with its N terminus toward the pointed end near the sarcomere's midpoint, the M-line. It is at the pointed end where the competition between Lmod and Tmod binding to Tpm takes place (Tolkatchev et al., 2020, 2021). When Lmod is bound, thin filaments are elongated (Tsukada et al., 2010; Mi-Mi et al., 2020; Tolkatchev et al., 2020; Larrinaga et al., 2024). On the other hand, when Tmod is bound through all its binding sites, it occludes the pointed end (Tolkatchev et al., 2021; Carman et al., 2023; Li et al., 2023). Tmod acts as a cap for the pointed end and no elongation or depolymerization of the thin filament is allowed (Weber et al.,

[1]Voiland School of Chemical Engineering and Bioengineering, Washington State University, Pullman, WA, USA; [2]Department of Medicine and Cardiovascular Research Institute, Icahn School of Medicine at Mount Sinai, New York, NY, USA; [3]Department of Cellular and Molecular Medicine and Sarver Molecular Cardiovascular Research Program, The University of Arizona, Tucson, AZ, USA.

*B. Osegueda, S. Minakhina, and N. Starks contributed equally to this paper. Correspondence to Alla S. Kostyukova: alla.kostyukova@wsu.edu; Garry E. Smith, Jr.: garry.smith@wsu.edu

N. Starks died on May 8, 2023.

This work is part of a special issue on Myofilament Structure and Function.

1994; Gregorio et al., 1995). Thin filaments must be elongated and maintained at mature lengths for efficient muscle contraction. Changes in the lengths can lead to cardiac and skeletal myopathies (Yuen et al., 2014; Pappas et al., 2015; Li et al., 2016; Winter et al., 2016; Pappas et al., 2018; Ahrens-Nicklas et al., 2019; Mi-Mi et al., 2020; Yuen et al., 2022; Sono et al., 2023; Vasilescu et al., 2024).

Lmod has three actin-binding sites and one Tpm-binding site, while Tmod has two actin-binding sites and two Tpm-binding sites (Fowler and Dominguez, 2017; Tolkatchev et al., 2022). A comparison of the Lmod and Tmod sequences has shown that there is a high level of homology (Tolkatchev et al., 2019). In major cardiac isoforms Lmod2 and Tmod1, their first Tpm-binding sites have 57% sequence identity and 78% sequence similarity, and it is this site that is suggested to govern their competition (Tolkatchev et al., 2020). Among all Tmod family proteins, Lmod2 has the highest affinity for striated muscle α-Tpm (Tpm1.1) in the Tpm-binding site 1 (Kostyukova, 2007 Uversky et al., 2011; Yuen et al., 2014), which enables Lmod2 to successfully compete for pointed end binding. Introducing an L25G mutation in Tpm-binding site 1 abolished Lmod2 binding to Tpm1.1 and drastically decreased its ability to compete Tmod1 off the pointed end, therefore leading to shortened thin filaments (Tolkatchev et al., 2020). Further examining the structural characteristics of the Lmod2/Tpm1.1-binding interface holds promise for shedding light on the intricate regulatory mechanisms governing thin filament length.

Hypomorphic mutations, which do not eliminate Lmod2's function but rather slightly attenuate it, can be used as a tool to demonstrate the effect of competition between Lmod2 and Tmod1. However, designing hypomorphic mutations is more challenging than designing mutations that destroy interactions. In this study, circular dichroism (CD) experiments were conducted to assess the effects of several mutations in the Tpm-binding site of Lmod2, which were predicted to be hypomorphic (i.e., E34Q, S24K, S24L, and E36V), on the stability of the complex formed between Lmod2s1 and αTM_{1-14}Zip. We measured the thermally induced denaturation of complexes between Lmod2s1, a fragment that contains the first 40 residues of Lmod2 representing the Tpm-binding site (with and without a mutation), and a Tpm1.1 model peptide, αTM_{1-14}Zip, which contains an Lmod2-binding site. The model peptide consists of the first 14 residues of Tpm1.1 fused to a GCN4 leucine zipper sequence at the C terminus and forms a coiled-coil dimer (Greenfield et al., 1998; Colpan et al., 2016). Employing various molecular dynamics simulations (MDS)-based approaches, the standard Gibbs free energies of binding were calculated for Lmod2s1 (WT and mutated) in complex with αTM_{1-14}Zip. A strong correlation was found between standard Gibbs free energies of binding and changes in melting temperatures (ΔT_m). Of these mutations, we tested the E34Q mutation in cardiomyocytes. The melting temperature (T_m) of the complex formed by Lmod2s1[E34Q] and αTM_{1-14}Zip was reduced by 2.9°C compared with the WT complex, indicating a slight decrease in the affinity of Lmod2 for Tpm1.1. When Lmod2 [E34Q] was expressed in isolated cardiomyocytes, it was largely unable to compete off Tmod1 at thin filament pointed ends. The E34Q mutation also significantly affected the ability of Lmod2 to elongate thin filaments. Our results highlight the essential role of the Tpm-binding site in the dynamic equilibrium between Tmod-1 and Lmod-2 at the pointed end of thin filaments and suggest the potential use of the correlation between standard Gibbs free energies of binding and ΔT_m to predict changes in the stability of complexes between Tpm and Lmod (Tmod) isoforms.

Materials and methods

Peptide design and plasmid preparation

The choice of Lmod2s1 and $\alpha TM1a_{1-14}$Zip sequences was described previously (Colpan et al., 2016). Briefly, Lmod2s1 contained the first 40 residues of Lmod2, representing the Tpm-binding site. $\alpha TM1a_{1-14}$Zip contained the first 14 residues of Tpm1.1 fused with 18 residues of GCN4 leucine zipper sequence at the C terminus to promote coiled-coil formation, which is a common practice in Tpm model peptides (Nitanai et al., 2007; Greenfield et al., 2009; Uversky et al., 2011).

Mutations were introduced into Lmod2s1 by PCR-based mutagenesis using partially overlapping primers (Table S1) ordered from Integrated DNA Technologies. The PCR reactions were performed with PfuTurbo DNA polymerase (Agilent), and the mutated plasmids were used to transform *Escherichia coli* DH5α (Life Technologies). The presence of each mutation was confirmed by Sanger sequencing (Genewiz).

Protein expression and purification

The mutated plasmids were used to transform *E. coli* BL21(DE3) (Life Technologies). Transformed cells were grown in LB media in the presence of 0.1 mg/ml ampicillin, and protein expression was induced with 0.1 mM IPTG. Purification was performed as described for Lmod2s1 (Colpan et al., 2016). Both $\alpha TM1a_{1-14}$Zip, acetylated at the N terminus, and Lmod2s1 with 11 truncated N-terminal residues were synthesized at the Tufts University Core Facility. Peptide concentrations were determined by measuring the difference spectra as described by Tolkatchev et al. (2020) and by the BCA method (Thermo Fisher Scientific).

CD

CD measurements were carried out using an Aviv model 420 spectropolarimeter in 1-mm cuvettes. Dynode voltage was below 500 V in all measurements. The protein concentration for the CD experiments was ~20 µM in 10 mM Na-phosphate, pH 7, and 100 mM NaCl. The melting curves were recorded at 222 nm by varying the temperature from 0 to 65°C with a temperature step of 0.2°C, a temperature deadband of 0.15°C, a 0.3-min equilibration time, and an averaging time of 5 s for each point. In each experiment, we used a 5-cuvette rotor to simultaneously measure the melting curves of WT (as a control) and mutated Lmod2s1 alone, $\alpha TM1a_{1-14}$Zip alone, and WT and mutated Lmod2s1 in complex with $\alpha TM1a_{1-14}$Zip. T_m of the complexes were determined by fitting the curves as described by Greenfield (2006); Uversky et al. (2011), and T_m of the WT complex was subtracted from T_m of the mutated complex from the same

measurement to obtain ΔT_m. The K_d was calculated using T_m and enthalpy obtained from the fitting, as described by Greenfield and Fowler (2002); Greenfield (2006); Kostyukova et al. (2007). An unpaired *t* test was used for statistical analysis.

MDS

For polypeptide structure visualization, we used the UCSF Chimera package (Pettersen et al., 2004). The initial structures of Lmod2s1 and αTM1a$_{1-14}$Zip were obtained from the known structure (PDB ID 6UT2). MDS were performed using AMBER22 (Case et al., 2022) for both the complex (Lmods1 and αTM1a$_{1-14}$ Zip) and each peptide in isolation. For MDS, we neutralized the structures by adding Na^+ ions in an optimal point charge water box (Izadi et al., 2014) with a minimum distance of 10 Å from the edge of the box. The force field used was the ff99SB (Hornak et al., 2006). Energy minimization and relaxation were performed to stabilize the structure and avoid atomic clashes. During minimization, positional restraints were applied with a restraint weight of 100 kcal/mol/Å. After minimization, the protein was slowly heated from 100 to 300 K while maintaining the same positional restraints. We then relaxed the positional restraints while introducing pressure control with the Monte Carlo barostat. For the production runs, no pressure control was applied. The temperature was controlled by a Langevin thermostat using a 3-ps^{-1} collision frequency. Hydrogens were constrained using SHAKE. We ran 1-µs–long MDS for WT and mutated Lmod2s1 peptides alone, αTM1a$_{1-14}$Zip alone, and the WT and mutated Lmod2s1/αTM1a$_{1-14}$Zip complexes, writing the trajectories every 50 ps, for a total of 20,000 frames.

Standard Gibbs free energy of binding calculation using the molecular mechanics Poisson–Boltzmann (generalized born) surface area

Within MDS by AMBER22, the most well-known approaches to evaluate the standard Gibbs free energy of binding, $\Delta G°_{bind}$, for a protein–protein complex are the molecular mechanics Poisson–Boltzmann surface area (MMPBSA) and MM generalized born SA (MMGBSA) methods (Srinivasan et al., 1998; Wang et al., 2019a). The standard Gibbs free energy of the non-covalent complex, PL, between components P and L is defined by

$$G°_{bind} = G^0_{PL} - G^0_P - G^0_L.$$

Here, G^0_P and G^0_L are the standard Gibbs free energies of unbound components P and L, whereas G^0_{PL} is the standard Gibbs free energy of the complex, PL. In MMPB(GB)SA, the standard Gibbs free energy of a state is estimated using the following equation (Kollman et al., 2000):

$$G^0 = E^0_{bond} + E^0_{angle} + E^0_{tors} + E^0_{vdw} + E^0_{elec} + G^0_{pol} + G^0_{np} - TS^0.$$

Here, E^0_{bond}, E^0_{angle}, E^0_{tors}, E^0_{vdw}, and E^0_{elec} are the bond, angle, torsion, Van der Waals, and electrostatic energies, respectively, which are calculated according to the molecular mechanics force field used in MDS, with no nonbonded cutoff. ΔG^0_{pol}, the polar solvation energy, is calculated with either the Poisson–Boltzmann or generalized born methods (Still et al., 1990; Honig and Nicholls, 1995). G^0_{np}, the nonpolar solvation term, is calculated using a solvent-accessible surface area algorithm (Sanner et al., 1996). TS^0 is the temperature-entropy product term, which is neglected in our model because our focus lies not on the absolute ΔG^0_{bind} but rather on the relative ΔG^0_{bind} between complexes with similar entropies. In cases such as this, the temperature entropy product can be neglected (for review, see Wang et al. [2019a]).

Testing single- and triple-trajectory approaches

G^0_P and G^0_L can be calculated either from structures of the components P and L obtained from an MDS trajectory of the complex, PL, which we refer to as the single-trajectory approach, or from structures of the components P and L obtained from MDS trajectories of the individual components P and L, which we call the triple-trajectory approach. For both approaches, G^0_{PL} is always calculated based on structures of the complex extracted from the MDS trajectory of the complex.

In the single-trajectory approach, G^0_P and G^0_L were calculated based on structures of αTM1a$_{1-14}$Zip and Lmod2s1, respectively, extracted from the Lmod2s1/αTM1a$_{1-14}$Zip complex trajectory only. This assumes that their structures do not change significantly between the bound and unbound states. However, since Lmod2s1 peptides gain α-helical content upon binding to αTM1a$_{1-14}$Zip, this assumption could lead to inaccuracies in the calculated standard free energy of binding.

In the triple-trajectory approach, G^0_P and G^0_L were calculated based on the structures of αTM1a$_{1-14}$Zip and Lmod2s1 extracted from the trajectories of αTM1a$_{1-14}$Zip and Lmod2s1 alone, respectively, which took into account changes in their structures in the bound and unbound states. We tested both approaches.

For the single-trajectory approach, we used the 1-µs trajectories of WT and mutated Lmod2s1/αTM1a$_{1-14}$Zip complexes. For the triple-trajectory approach, we used the 1-µs trajectories of WT and mutated Lmod2s1 peptides alone, αTM1a$_{1-14}$Zip alone, and WT and mutated Lmod2s1/αTM1a$_{1-14}$Zip complexes. Each 1-µs trajectory consisted of 20,000 frames. We initially used a sampling interval of 50 for a total of 400 frames for both the MMPBSA and the MMGBSA models and with both the single-trajectory and the triple-trajectory approaches to calculate the standard free energy of binding (Table S2). The results from MMPBSA and MMGBSA were compared with the ΔT_m from the CD experiments. Plotting ΔT_m versus ΔG^0_{bind} allowed us to calculate the coefficient of determination, R^2, value with a linear fit using SigmaPlot (Table S3). We then selected the model with the higher R^2 value. In our case, it was the MMPBSA triple-trajectory approach. We then proceeded with the MMPBSA triple-trajectory approach, with sampling intervals of 5- and 10-ns steps and an internal dielectric constant (ε) of 2 or 1 (Table S4). The sampling interval of 10 ns and ε = 1 gave the best fit.

Virus preparation for expression of GFP-Lmod2[E34Q]

mLmod2 was cloned into pEGFP-C2 vector (Clontech) to create GFP-mLmod2 expression plasmids. The E34Q mutation was introduced using a QuikChange site-directed mutagenesis kit (Strategene). All sequences were confirmed by DNA sequencing. Adenovirus-expressing GFP, GFP-mLmod2, and GFP-mLmod2 [E34Q] were constructed into a replication-deficient Adv vector using the AdEasy Adenoviral Vector System (Agilent

Technologies) as described by Pappas et al. (2015). Briefly, GFP construct cDNA was subcloned into a pShuttle-CMV plasmid and linearized before transformation of BJ5183 cells containing the pAdEasy-1 vector. After homologous recombination, the purified pAdEasy-1 vector containing either GFP, GFP-mLmod2, or GFP-mLmod2 [E34Q] was transfected into HEK293 cells for Adv propagation. The Adv then was purified by CsCl gradient centrifugation, and viral titer was determined by a dilution assay in HEK293 cells grown in 96-well plates. At a MOI of 5–10, ∼90% of cardiomyocytes were transfected, as determined by GFP-positive cells.

Expression of GFP-Lmod2 in neonatal cardiomyocytes

Rat neonatal cardiomyocytes were isolated from postnatal day 1–3 Sprague–Dawley rat (Charles River Laboratories) hearts as described (Gustafson et al., 1987). All animal experiments were approved by the Institutional Animal Care and Use Committee of the University of Arizona (#08–017; protocol). All experiments were performed in compliance accordance with the ARRIVE guidelines and in accordance with the Institutional Animal Care and Use Committee regulations, which meet recommendations in the Guide for the Care and Use of Laboratory Animals of the National Institutes of Health and Public Health Service Policy on Humane Care and Use of Laboratory Animals (Department of Agriculture, Animal Welfare Act).

Isolated cells were plated on 35-mm tissue culture dishes containing 12-mm round glass coverslips thin-coated with Matrigel (1:100; BD Biosciences) at ∼4.5 × 10^5 cells/dish. Cells were maintained in DMEM with 1 g/liter glucose (Life Technologies) with the addition of 10% (vol/vol) fetal bovine serum (HyClone) and 1% penicillin-streptomycin (Cellgro; Mediatech). Cardiomyocytes were transduced with adenovirus 2 d after plating with 2–5 MOI of adenovirus as described by Pappas et al. (2015), which increases intracellular Lmod2 levels on average 40%. To achieve similar levels of protein expression, GFP fluorescence in cardiomyocytes of each experimental group was inspected using Nikon Eclipse T*i* microscope (see below), and average fluorescent intensity was measured for at least 100 cells per culture.

Cardiomyocyte imaging and analysis

At 2 d after transduction, cells were incubated in relaxing buffer (150 mM KCl, 5 mM $MgCl_2$, 10 mM 3-[*N*-morpholino] propanesulfonic acid, pH 7.4, 1 mM EGTA, and 4 mM ATP) for 15 min and fixed with 2% paraformaldehyde in relaxing buffer for 15 min. To determine whether specific proteins were tightly associated with the Triton X-100 insoluble (i.e., cytoskeletal/sarcomeric) fraction, cells were extracted in cytoskeleton-stabilization buffer (10 mM 1,4-piperazinediethanesulfonic acid, pH 6.8, 100 mM KCl, 300 mM sucrose, 2.5 mM $MgCl_2$, and 0.5% Triton X-100 plus protease inhibitors) before fixation. Following fixation, cells were permeabilized with 0.2% Triton X-100/PBS for 20 min at room temperature and then blocked with 2% BSA plus 1% normal donkey serum/PBS for 1 h at room temperature. Cardiomyocytes were stained as described (Pappas et al., 2015) with rabbit polyclonal anti-Tmod1 antibodies (2 µg/ml), monoclonal anti-GFP antibodies (11814460001; Sigma-Aldrich), and Texas Red–phalloidin (1:200; Invitrogen) to stain F-actin. Alexa Fluor 488 goat anti-mouse IgG (1:400), Alexa Fluor 647–conjugated donkey anti-rabbit IgG (1:400), or Alexa Fluor 350-conjugated donkey anti-rabbit IgG (1:400) secondary antibody was used. Cells were mounted onto slides with Aqua Poly/Mount (Polysciences). Images were captured using a Nikon Eclipse T*i* microscope with a 100× NA 1.5 objective, and a digital complementary metal oxide semiconductor camera (ORCA-flash 4.0; Hamamatsu Photonics). 3D deconvolution was performed using NIS offline deconvolution software (Nikon Corporation). To minimize bias, each microscopy field was systematically inspected for GFP-expressing cardiomyocytes. The same exposure/intensity parameters were used to acquire images within each experiment. Cardiomyocytes with low (<125 arbitrary units) or high (>1,500 arbitrary intensity) GFP intensity levels were excluded from analysis. Cardiomyocytes with similar levels of expression of GFP, GFP-Lmod2 [WT], or GFP-Lmod2 [E34Q] (Fig. S1 A) were used for Tmod1 assessments and thin filament measurements. Thin filament lengths and sarcomere lengths were measured blindly using the DDecon plugin (Gokhin and Fowler, 2017) for ImageJ (Schneider et al., 2012). Over 120 cells were analyzed per treatment group, with each datapoint on the graph representing an average of three measurements from individual cells. Statistical analysis was done using a one-way ANOVA with Prism 10.1.2 software (GraphPad Software).To differentiate the effect of Lmod2 overexpression on sarcomere and thin filament lengths, the relationship between these lengths (Fig. S1 C, scatter plot of individual measurements) was analyzed as described by Pappas et al. (2018). For determining thin filament pointed-end assembly of Tmod1, positively transfected cardiomyocytes (with regular striations) were classified as either "consistent" with well-defined striated Tmod1 staining at pointed ends with little cytoplasmic background or "inconsistent" with <50% Tmod1 striated staining at pointed ends, compared with non-transfected cells in the same sample (Fig. 5 C and Fig. S1 F [Tolkatchev et al., 2020]). 80–100 cells per culture were counted. Experiments were repeated three times. Statistical analysis was done using a one-way ANOVA with Prism 10.1.2 software (GraphPad Software). The data are presented as the percentage of the total number of mature GFP-positive cardiomyocytes in each group (mean ± SD). Data are from three independent cultures.

Images were also acquired with a Zeiss LSM980 microscope (Carl Zeiss Microscopy GmbH) equipped with GaAsP PMT detectors (Hamamatsu Photonics) in confocal mode. Imaging was performed using a 63×/1.4 Plan-Apochromat objective (Carl Zeiss Microscopy GmbH). Acquisition was performed in line scan mode, with a pixel dwell time of 1.02 ms/pixel and a frame average of 4. Excitation lasers used were 488 nm for GFP and Alexa Fluor 488 and 594 nm for Texas Red and Alexa Fluor 647, collected through an MBS488/561 double dichroic detector (Chroma Technology). For each experimental group, GFP-Lmod2[WT] was set as the experimental positive control to set the excitation parameters (laser power, detector gain) to provide the best signal-to-noise ratio for each chromophore, utilizing the full dynamic range of the detector and avoiding detector saturation. The settings determined for the positive control for each chromophore and experiment were used to acquire the rest of the cohort images.

Online supplemental material

Fig. S1 shows the analysis of WT and E34Q Lmod2 expression in cardiomyocytes. Fig. S2 shows the alignment of the complex structures before and after MDS. Table S1 lists the primers used to introduce mutations. Table S2 provides the calculated Gibbs free energy of binding with the 20-ns step interval. Table S3 and Table S4 provide the R^2 obtained from a linear fit of the plots obtained for different models and ε. Table S5 provides the K_d calculated from the unfolding curves.

Results

Selection of mutations with a spectrum of effects on the stability of the Lmod2s1/αTM1a$_{1-14}$Zip complex

Mutations in the Tpm-binding site of Lmod2 abolishing its binding to Tpm1.1 also eliminated its ability to compete with Tmod1 (Tolkatchev et al., 2020). However, to better understand the regulation of thin filament lengths, it is important to study how fine-tuning of the Lmod2/Tpm1.1-binding affinity affects competition between Lmod2 and Tmod1. Testing hypomorphic mutations with a range of affinities would be informative to determine the affinity-specific interactions responsible for Lmod/Tmod competition and thin filament elongation. Based either on the structure of the Lmod2/Tpm1.1-binding interface or on the comparison of Lmod isoform sequences, we selected mutations that are expected to moderately affect the affinity of Lmod2 for Tpm1.1.

The structure of the complex between Lmod2s1, a peptide representing the Tpm-binding site in Lmod2, and αTM1a$_{1-14}$Zip, a model peptide containing the N-terminal 14 residues of Tpm1.1 and a GCN4 leucine zipper to stabilize coiled-coil formation (Tolkatchev et al., 2020) (Fig. 1 A), was used for the first approach. Based on the NMR spectral data, the first 11 residues of Lmod2s1 remain disordered in the complex, while the remainder of Lmod2s1 forms an α–α hairpin connected by a two-residue turn and binds to the N terminus of αTM1a$_{1-14}$Zip, forming a hydrophobic core as well as several salt bridges.

Using static 3D structural information alone, we designed several mutations, S24K, S24L, and E36V, that we expected to slightly stabilize the complex. The S24K mutation was expected to stabilize the turn by the formation of a new salt bridge (Fig. 1 A). S24L was expected to increase the complex stability by adding hydrophobic interactions in the turn of Lmod2s1 positioned over the N terminus of the coiled-coil αTM1a$_{1-14}$Zip (Fig. 1 A). Since the side chain of E36 is close to the hydrophobic core, the E36V mutation was expected to contribute to hydrophobic interactions, therefore increasing the complex stability (Fig. 1 A).

For another approach, we compared sequences of Lmod isoforms. It was demonstrated that the binding of Tpm1.1 to Lmod3, the skeletal muscle-predominant Lmod isoform, is weaker than the binding of Tpm1.1 to Lmod2 (Yuen et al., 2014). We compared the sequences of the Tpm-binding sites for Lmod2 and Lmod3 to identify changes in Lmod2's Tpm-binding site that can alter the binding affinity to Tpm1.1 without destroying the interaction. Most of the residues in the Tpm-binding sites of Lmod2 and Lmod3 are identical or similar (Fig. 1 B). Residues S26–E41 form an α-helix in the C-terminal region of the Tpm-binding site. Of these residues, 10 are identical and 6 (E34, R35, L37, D39, I40, and E41) are different from Lmod3's sequence. To introduce a mutation that would make Lmod2's affinity for Tpm1.1 slightly lower than that of Tmod1 for Tpm1.1 without destroying Lmod2 interaction with Tpm1.1, we selected to change Glu34 in Lmod2 (Fig. 1 A) to Gln, present in a corresponding position of Lmod3.

Effects of the mutations on Lmod2 binding to Tpm1.1

The mutations were introduced in Lmod2s1, and the mutated peptides were purified. To test the affinity of the mutated peptides, we studied complex formation between WT and mutated Lmod2s1 and αTM1a$_{1-14}$Zip using CD. The prominent minimum in CD spectra for α-helical proteins is at 222 nm. Therefore, we measured the dependence of ellipticity at 222 nm on temperature. Lmod2s1, an intrinsically disordered peptide, gained α-helical content upon binding to αTM1a$_{1-14}$Zip (Kostyukova, 2007). First, we determined the effect of the E34Q mutation on Lmod2s1 binding to αTM1a$_{1-14}$Zip. We measured and compared the thermally induced unfolding of αTM1a$_{1-14}$Zip in complex with WT Lmod2s1 or the mutated Lmod2s1[E34Q] (Fig. 2). From the thermal unfolding curve, we determined the T_m, which is used as a characteristic of the complex stability. A weaker complex interaction should result in lower T_m, and a more stable complex should have higher T_m. We expected that the E34Q mutation would decrease the complex stability, and indeed, the T_m of the complex with Lmod2s1[E34Q] was 2.9°C lower than that for the WT (Fig. 2 B).

To test other mutations, we used the same thermal unfolding approach by CD as we did for the E34Q mutation. The mixtures of αTM1a$_{1-14}$Zip with each mutant showed an increase in helical content compared with the sum of the individual melting curves, which indicated binding. For each mutant, we determined a ΔT_m between the complex formed by WT and the mutated Lmod2s1 measured in the same experiment (for details, see Materials and methods, section CD) (Fig. 3). The mutations' impact on binding was not drastic, yet they did have a range of effects on T_m (Table 1); however, while we expected that three mutations, S24K, S24L, and E36V, would increase T_m, only the E36V mutation resulted in an increase of T_m. The differences in T_m between WT and the mutated fragments were statistically significant for the E34Q and E36V mutations (Table 1).

Standard free energies of binding correlated with ΔT_m

Not all mutations we designed based on the static 3D structure had the expected effects. Therefore, to improve the predictability of modeling the affinity change, we used MDS to consider atomic motions. MDS stands as a potent technique for estimating the affinities of protein–protein interactions through the calculation of standard Gibbs free energies of binding (Wang et al., 2019a, 2019b). In this regard, we introduced the mutations (E34Q, S24L, E36V, and S24K) in silico using UCSF Chimera, a program for interactive visualization and analysis of molecular structures (Pettersen et al., 2004) with the PDB ID 6UT2 as a template structure. PDB files for each of the Lmod2s1 mutants were prepared alone and in complex with αTM1a$_{1-14}$Zip. To run MDS, we used the ff99SB force field, a collection of

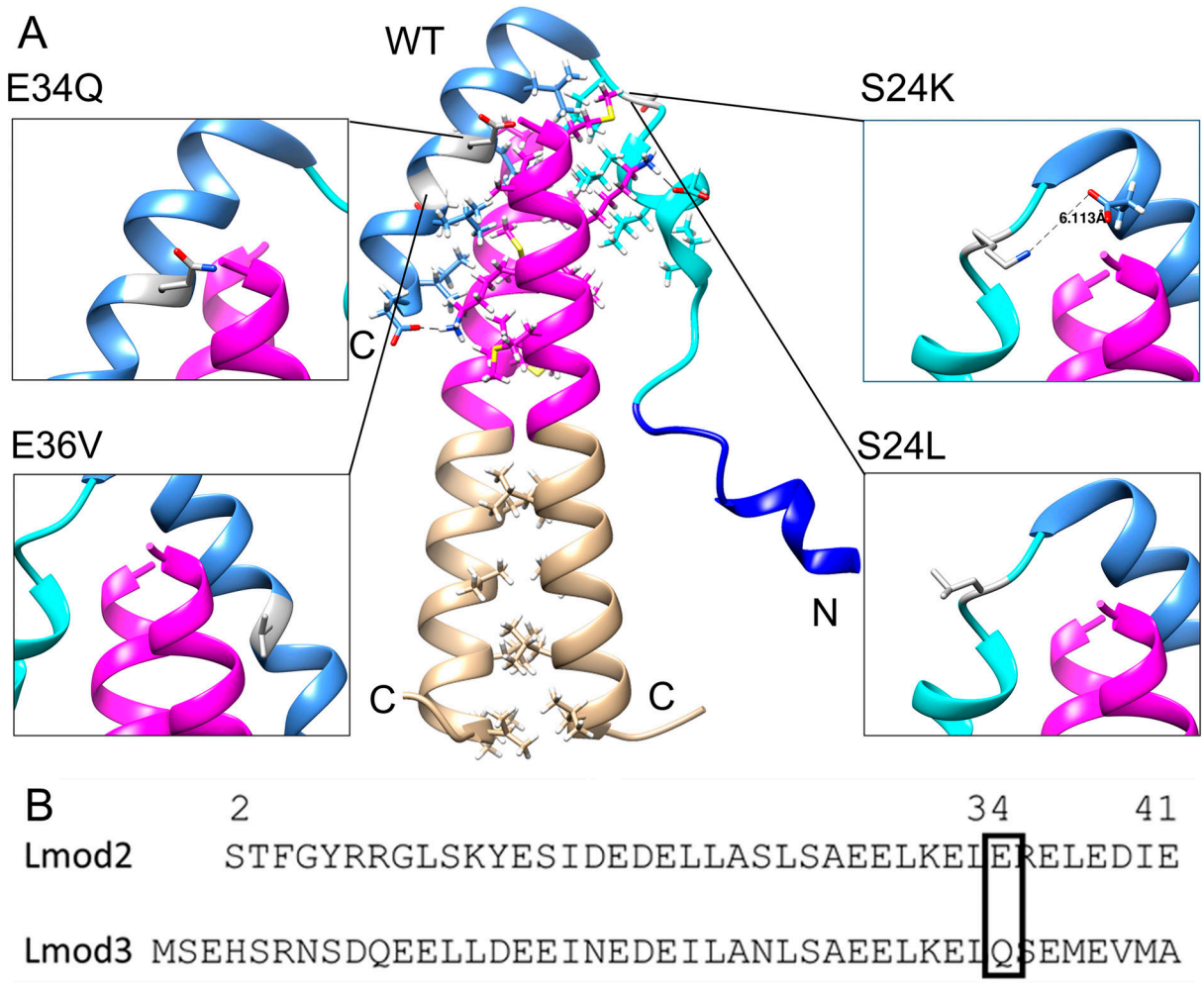

Figure 1. **Positions of the mutations. (A)** Structure of Lmod2s1/αTM1a$_{1-14}$Zip complex (PDB ID 6UT2). The section in magenta is the first 14 residues of the Tpm1.1 fragment. The section highlighted in tan is the leucine zipper sequence. The section highlighted in blue is the first 11 residues of the Lmod2 fragment, which were removed in the Δ11 mutation. The section highlighted in cyan represents residues 12–25 of Lmod2s1, and the section highlighted in cornflower blue is the remainder of Lmod2s1 (residues 26–41). The mutated residues are shown in gray, with side chains displayed for clarity. The side chains of all residues that form the hydrophobic core of the complex are shown in the central image, as well as two salt bridges formed by Lmod2's Asp19 and Glu41 with lysine in αTM1a$_{1-14}$Zip. The N and C termini of the Lmod2s1 and the C termini of the αTM1a$_{1-14}$Zip dimer are labeled. Inserts show magnified views of the complex in the region of the mutations S24K, S24L, E36V, and E34Q, introduced in Chimera and before MDS. **(B)** Comparison of the sequences of the Tpm-binding sites for Lmod2 and Lmod3 (a skeletal muscle isoform).

parameters essential for delineating the evolution of bond lengths, angles, and intermolecular interactions (Freddolino et al., 2009). Different force fields employ distinct equations and constants to accurately model the geometrical configurations and properties of molecules, and the FF99SB force field, in combination with the optimal point charge rather than the TIP3P water model, is better suited for intrinsically disordered proteins (Shabane et al., 2019). With the selected parameters, we aimed to test the correlation between the stability of the complexes formed by αTM1a$_{1-14}$Zip and Lmod2s1 with various mutations and standard free energies of binding.

We ran 1-μs simulations of αTM1a$_{1-14}$Zip, WT Lmod2s1, and each mutated Lmod2s1 alone and in complex. Using the MMPBSA model with a triple-trajectory approach, an internal ε of 1, and a sampling interval of 200 for a total of 100 frames, which was chosen after extensive testing (for details see Materials and methods, section Testing single- and triple-trajectory models), we calculated the $\Delta G°_{bind}$ for each Lmod2s1/αTM1a$_{1-14}$Zip complex (Table 2). The calculated standard free energies of binding for each mutant were plotted against their ΔT_m (Fig. 4 A), and the R^2 with a linear fit was calculated to be 0.93.

To assess how a mutation involving more than a single residue change would affect our calculations, we investigated the results of truncating the 11 N-terminal residues (Δ11) in Lmod2s1 both by CD and MDS. Since the first 11 residues of Lmod2s1 may interact with αTM1a$_{1-14}$Zip only transiently (Fig. 1 A), we expected that this would slightly decrease the complex stability; however, there was almost no effect of the truncation on the complex T_m (Table 1 and Fig. 3). When we included the results for Δ11 mutation (Fig. 4 B), the calculated R^2 was 0.40. The point corresponding to the Δ11 mutation

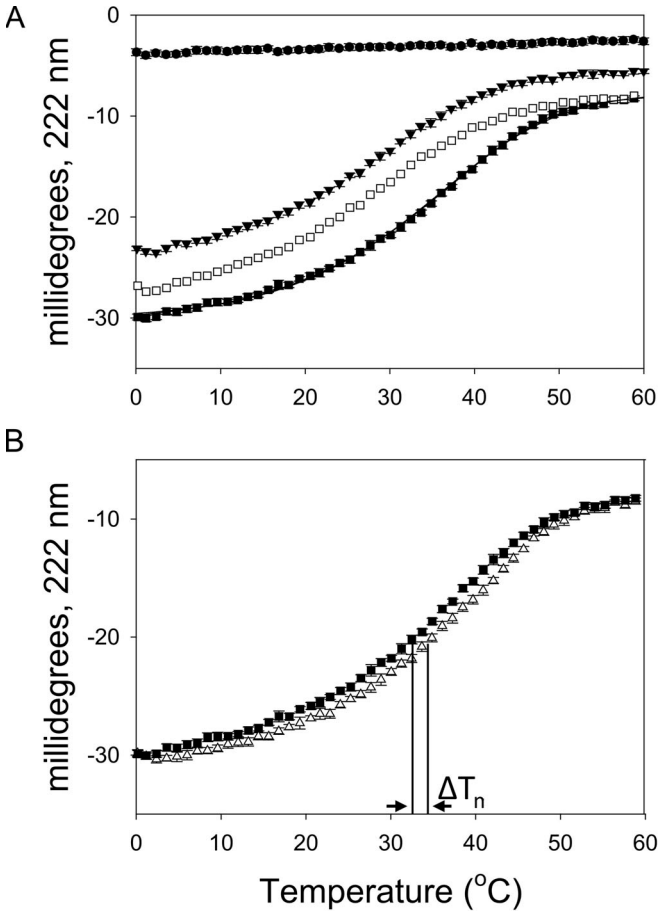

Figure 2. **The E34Q mutation in the Tpm-binding site of Lmod2 slightly decreases the binding affinity to Tpm1.1. (A)** Representative measurements showing the temperature dependence of the ellipticity at 222 nm measured for unmixed and mixed αTM1a$_{1-14}$Zip and Lmod2s1: Lmod2s1 [E34Q] (●), αTM1a$_{1-14}$Zip (▼), a mixture of Lmod2s1[E34Q] and αTM1a$_{1-14}$ Zip (■), and a sum of the individual curves for Lmod2s1[E34Q] and αTM1a$_{1-14}$Zip (□). **(B)** The temperature dependence of the ellipticity at 222 nm measured for mixtures of αTM1a$_{1-14}$Zip with Lmod2s1[WT] (Δ) and Lmod2s1[E34Q] (■). Each data point represents a 5-s average of the signal, with SEM shown as bars.

contributed most to the error, and its position on the plot was farthest from the fit.

Based on our results, the correlation between standard free energies of binding and ΔT_m is better suited to predict the effects of point mutations rather than truncations or other large changes. This approach can be used to predict changes in the stability of the complexes between Tmp and Lmod (Tmod) isoforms for further studies of dynamic equilibrium between Tmod and Lmod at the pointed ends of thin filaments.

Lmod2 E34Q assembles similarly to WT, does not displace Tmod1, and has reduced ability to elongate thin filaments compared with WT

Based on both sequence-dependent prediction and the CD data, Lmod2[E34Q], which exhibited lower affinity for Tpm1.1, was an ideal candidate for testing the competition between Lmod2 and Tmod1 for binding at the pointed end of the thin filament in cells. We were interested in examining how altering the binding affinity, such that Lmod2's affinity for Tpm1.1 at this site becomes slightly lower than that of Tmod1, would affect the localization of Lmod2 and Tmod1 in cells. Our selection was based on the fact that, among all the mutations that decreased affinity, E34Q was the only one that suggests biological function—Lmod3 naturally contains Gln at this position instead of Asp—and the change in T_m was statistically significant.

We compared K_d for complexes formed by αTM1a$_{1-14}$Zip and peptides representing the Tpm-binding site 1 of Lmod2 and Tmod1. K_d can be calculated from thermodynamic parameters, such as T_m and enthalpy, obtained from melting curves recorded by CD (Kostyukova et al., 2007). Previous studies have shown that the K_d for the Lmod2s1/αTM1a$_{1-14}$Zip complex is slightly lower than that for the Tmod1s1/αTM1a$_{1-14}$Zip complex (0.8 ± 0.2 μM [Kostyukova, 2007] and 1.1 ± 0.4 μM [Uversky et al., 2011], respectively). The higher affinity of Lmod2 for Tpm1.1 aligns with its ability to displace Tmod1 from the pointed ends of thin filaments when expressed in cardiomyocytes (Tolkatchev et al., 2020).

Using the same approach, we calculated the K_d for Lmod2s1 [E34Q]/αTM1a$_{1-14}$Zip complex as 1.35 ± 0.8 μM. This was still lower than the K_d = 3.5 ± 0.5 μM for the Lmod3s1/αTM1a$_{1-14}$Zip complex (Yuen et al., 2014), indicating that the residue in position 34 was not the only contributor to the difference in binding affinity between Lmod2 and Lmod3 for Tpm1.1. However, the K_d for Lmod2s1[E34Q]/αTM1a$_{1-14}$Zip complex was higher than K_d = 1.1 ± 0.4 μM for the Tmod1s1/αTM1a$_{1-14}$Zip complex, indicating that the E34Q mutation made the affinity of Lmod2 to Tpm1.1 slightly lower than that of Tmod1.

Overexpression of Lmod2 in cardiomyocytes leads to displacement of Tmod1 from the pointed ends of thin filaments (Tsukada et al., 2010; Tolkatchev et al., 2020). To test if shifting of Lmod2 affinity for Tpm1.1 to a slightly lower affinity affects the ability of Lmod2 to bind thin filaments and compete off Tmod1, we expressed GFP, GFP-Lmod2, and GFP-Lmod2[E34Q] via adenovirus in rat neonatal cardiomyocytes (Fig. 5 and Fig. S1). Infected cells were stained for endogenous Tmod1. Cardiomyocytes expressing GFP alone demonstrated consistent striations of Tmod1 assembly at pointed ends (~85%, Fig. 5, A and B), comparable with that observed in noninfected cells in the same culture. GFP-Lmod2 and GFP-Lmod2[E34Q] were expressed at similar levels (Fig. S1). Overexpression of GFP-Lmod2[WT] significantly decreased the percentage of cells demonstrating a consistent pointed-end assembly pattern of Tmod1 (i.e., Tmod1 was competed off the ends) (~40%, $P < 0.0001$), while expression of GFP-Lmod2[E34Q] did not have a significant effect on Tmod1 assembly compared with GFP controls (~75% cells with consistent Tmod1 striated staining, $P = 0.0502$, Fig. 5 B). This alteration in assembly resembled the effect of the L25G mutation in Lmod2 Tpm-binding site, which effectively disrupted Lmod2s1/αTM1a$_{1-14}$Zip (Tolkatchev et al., 2020). However, unlike GFP-Lmod2[L25G], the GFP-Lmod2[E34Q] showed consistent localization on thin filament pointed ends (Fig. 5, A and C). To differentiate between strong and loose association of Lmod2 and Tmod1 with the detergent-insoluble cytoskeletal fraction (i.e., thin filament), we treated isolated cardiomyocytes with a Triton

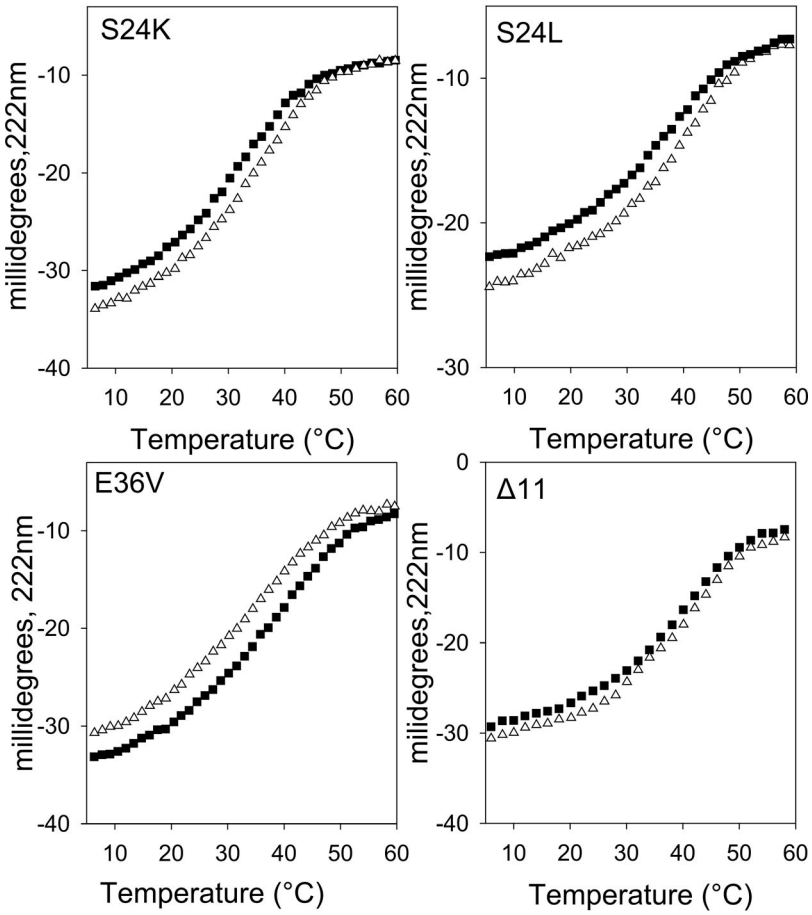

Figure 3. **Effect of the mutations in Lmod2s1 on unfolding of its complex with αTM1a$_{1-14}$Zip.** Representative measurements for the complexes with mutated Lmod2s1, showing the temperature dependence of the ellipticity at 222 nm measured for mixtures of αTM1a$_{1-14}$Zip with WT (Δ) or mutated (■) Lmod2s1.

X-100 containing cytoskeleton-stabilization buffer to remove cytosolic and weakly bound cytoskeletal-associated proteins (see Materials and methods, section Cardiomyocyte imaging analysis). This treatment efficiently removed most GFP from GFP-alone infected (control) cardiomyocytes but preserved the localization of GFP-Lmod2, both WT and E34Q, at the pointed ends (Fig. 5 C). Importantly, this treatment did not visibly disturb Tmod1 assembly at pointed ends of thin filaments in cells expressing GFP or GFP-Lmod2[E34Q] (Fig. 5 C and Fig. S1 F), indicating that even in excess of the Lmod2 mutant, Tmod1 remains associated with the thin filament.

Table 1. **The difference between the melting temperatures, ΔT$_m$, of αTM1a$_{1-14}$Zip in complex with WT and mutated Lmod2s1**

Fragment	ΔT$_m$ (°C)	P Value
Lmod2s1 [E34Q]	−2.9 ± 0.9	0.0228
Lmod2s1[S24K]	−1.4 ± 0.9	0.1588
Lmod2s1[S24L]	−2.8 ± 1.0	0.0583
Lmod2s1[E36V]	2.5 ± 0.8	0.0476
Lmod2s1Δ11	0.3	ND

To compare with WT, P values were calculated using an unpaired *t* test (*n* = 2, 2, 2, and 3 for S24K, S24L, E36V, and E34Q, respectively; *n* = 1 for Lmod2s1Δ11).

As expected, GFP-Lmod2 overexpression led to increased thin filament lengths compared with the expression of GFP alone (0.87 and 0.75 µm, respectively, P < 0.0001). GFP-Lmod2[E34Q] was also able to elongate thin filaments, consistent with its largely preserved ability to bind Tpm1.1 and pointed ends of thin filaments. However, the filaments in GFP-Lmod2 [E34Q]–expressing cells were significantly shorter compared with cells expressing similar levels of WT GFP-Lmod2 (0.83 and 0.87 µm, respectively, one-way ANOVA P < 0.0001, Fig. 5 D, or nested one-way ANOVA P = 0.0381, Fig. S1 E). This observation is consistent with the presence of Tmod1 at pointed ends (inability of Lmod2 to compete it off the pointed ends) and its partially preserved ability to inhibit pointed end elongation.

Table 2. **ΔG°$_{bind}$ calculated from the 1-µs simulation production run using MMPBSA with a 10-ns step interval**

Fragment	ΔG°' (kcal/mol)
Lmod2s1[WT]	−17.5
Lmod2s1[E34Q]	0.74
Lmod2s1[S24K]	−12.2
Lmod2s1 [S24L]	−3.13
Lmod2s1[E36V]	−24.3
Lmod2s1Δ11	−56.2

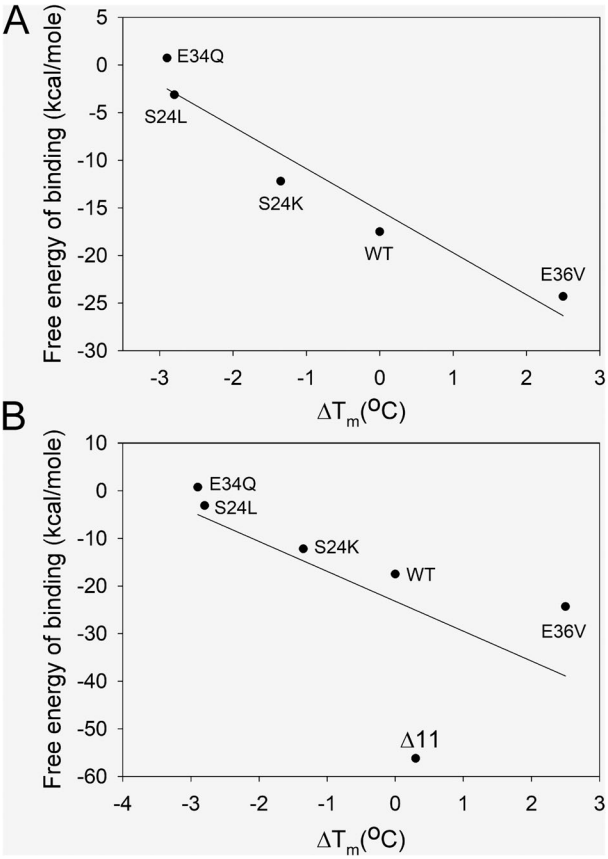

Figure 4. **Correlation between standard free energies and ΔT_m. (A)** Plot of standard free energy of binding versus ΔT_m for E34Q, S24K, E36V, and S24L. **(B)** Plot of standard free energy of binding versus ΔT_m for E34Q, S24K, E36V, S24L, and Δ11. ΔT_m for WT is 0. Lines represent a linear fitting.

Discussion

Our research aimed to investigate the regulatory mechanisms of thin filament length in striated muscles by studying mutations that alter Lmod2's affinity for Tpm1.1 while preserving their interaction. The first objective of this study was to assess whether there is a correlation between computational and biochemical results, with the goal of predicting biochemical characteristics, such as affinity, based on simulation data.

We determined the effects of several mutations in the Tpm-binding site of Lmod2 on its affinity to Tpm1.1 through a combination of CD and MDS techniques and developed a model to predict affinity changes that outperformed attempts based solely on the known structure of the binding interface. MDS results depend on how the studied system matches the available model, and experimental confirmation is required for model validation. Our goal was to combine the use of simulations with in vitro experiments to determine what models and parameters are best for the studied system. We used several mutations, E34Q, S24K, E36V, and S24L, as well as truncation of the 11 N-terminal residues of Lmod2, which have subtle effects or no effect at all on Lmod2s1/αTM1a$_{1-14}$Zip complex stability.

The complexes exhibited considerable dynamics along the MDS trajectories. Additionally, some mutations had a long-range influence on the interface structure. Therefore, visual evaluation of the final simulated structures (Fig. S2) and identifying the breakage of static interactions for those structures only were not appropriate for assessing mutation-induced stability changes. To address this, we evaluated stability by calculating the $\Delta G°_{bind}$. After testing several options of the MMPB(GB)SA model, we were able to improve the R^2 of the model to 0.93 with the Poisson–Boltzmann triple-trajectory model. The MMPBSA method requires structures of both proteins in a complex in the unbound and bound state to calculate binding free energy. These structures can be obtained from a single MDS trajectory of the proteins in complex, called the single-trajectory approach, which assumes that the conformation of both proteins is the same in the bound and unbound states. These structures can also be obtained from MDS trajectories of the proteins in complex and from both proteins in isolation, called the triple-trajectory approach, which takes into account conformational changes upon binding. After testing both approaches, we found that the triple-trajectory approach resulted in a better correlation between calculated standard free energies of binding and experimental ΔT_m's. This can be explained by the fact that Lmod2s1 is mostly disordered when it is unbound, becoming more α-helical upon binding to αTM1a$_{1-14}$Zip. The triple-trajectory approach, by accounting for this conformational change, can more accurately calculate the standard free energy of binding of the Lmod2s1/αTM1a$_{1-14}$Zip complex.

Using thermodynamic parameters obtained from the CD melting curves (Greenfield, 2006), we calculated the K_d for complexes of all mutated Lmod2s1 and αTM$_{1-14}$Zip (Table S5), except the truncated one, which showed virtually no difference compared with WT. All K_d values were higher than that for WT Lmod2s1, indicating the decrease in affinity. However, the K_d calculated for Lmod2s1[E36V]/αTM$_{1-14}$Zip complex contradicted ΔT_m obtained for this mutation. While ΔT_m indicated the increase in stability, the calculated K_d was higher than that for Lmod2s1/αTM$_{1-14}$Zip complex. This discrepancy was the reason why we chose to use ΔTm to study the correlation between the standard free energy of binding and the stability of the complexes. The model-based approach developed by Greenfield (Greenfield and Fowler, 2002; Greenfield, 2006) depends on accurately determined concentrations for calculating K_d. Therefore, even a 15–20% error in concentration determination, which is typical for many methods, can result in significant differences in the values. In contrast, ΔT_m in our experiments was independent of concentration. Our measurements were performed on samples measured simultaneously in the 5-cuvette holder, and the amount of αTM$_{1-14}$Zip added to all cuvettes with the complex (WT or mutated Lmod2s1) was exactly the same as in the sample with the αTM$_{1-14}$Zip alone.

Our computational analyses revealed a correlation between the calculated standard free energies of binding and the ΔT_m obtained in CD experiments, highlighting the predictive power of our approach in understanding the effects of point mutations on the stability of Lmod2/Tpm1.1 complex. The PB model with triple trajectory has enough sensitivity to predict slight changes in complex stability. Using a step size of 5 ns for 1-μs simulation can be computationally expensive. However, we found that the

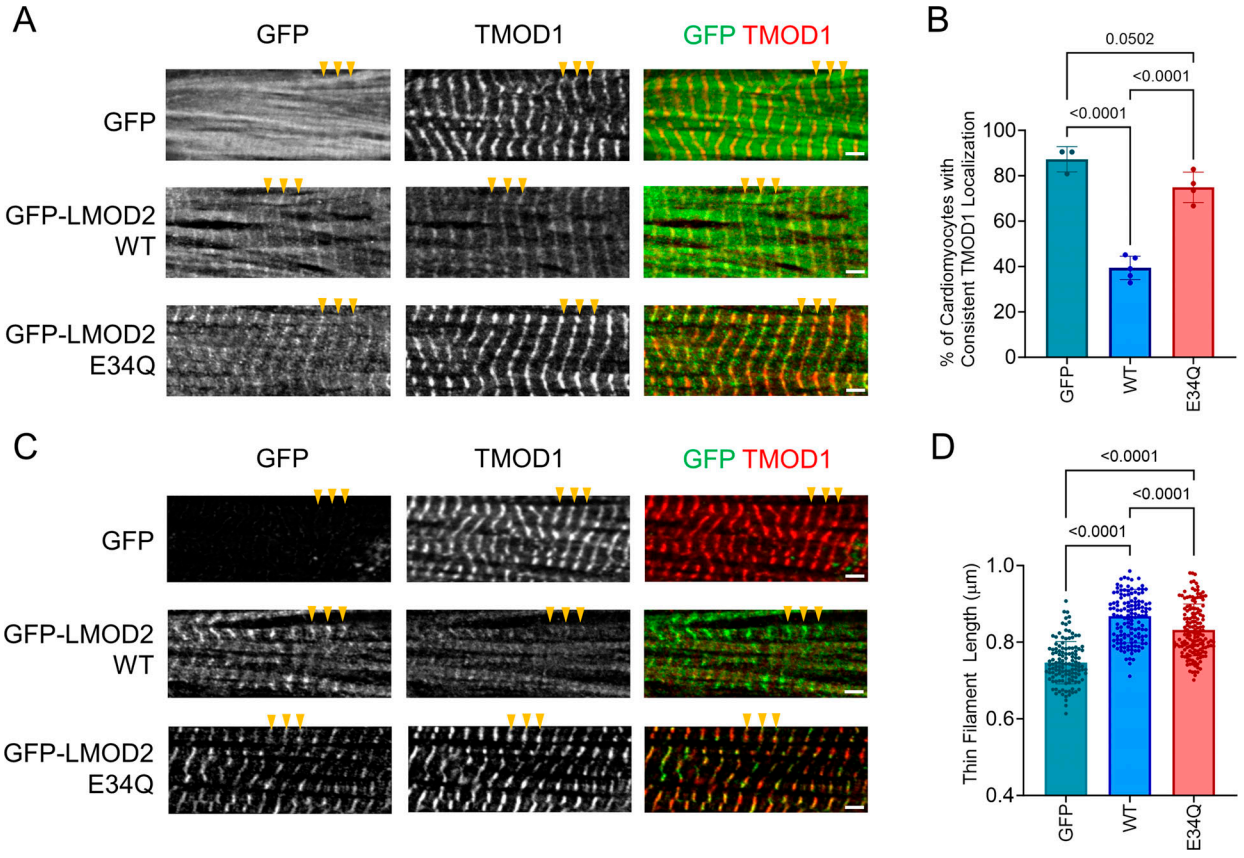

Figure 5. **Lmod2[E34Q] assembles at thin filament pointed ends, does not significantly displace Tmod1 from the pointed ends, and reduces ability to elongate thin filaments compared with WT Lmod2. (A)** Representative images showing Tmod1 assembly (red) in rat neonatal cardiomyocytes expressing (from top to bottom) GFP, GFP-Lmod2[WT], and GFP-Lmod2[E34Q] (green). **(B)** Percentage of cells with consistent Tmod1 assembly at pointed ends in cardiomyocytes expressing GFP (turquoise), GFP-Lmod2[WT] (WT, blue), and GFP-Lmod2[E34Q] (E34Q, red). Overexpression of WT Lmod2 caused significant displacement of Tmod1 from thin filament pointed ends. Similar levels of Lmod2[E34Q] (see Fig. S1 A) did not change Tmod1 distribution compared with GFP-expressing controls. **(C)** Samples extracted with a Triton-X–containing (cytoskeletal-extraction: CSK) buffer show a strong association of Tmod1 with pointed ends in the presence of GFP-Lmod2[E34Q], similar to that in GFP-expressing controls. (Note that GFP alone is substantially removed by CSK buffer treatment, as is the cytoplasmic and side binding for WT Lmod2 and Lmod2 E34Q). GFP-Lmod2 [E34Q] showed good association with pointed ends of thin filaments. Pointed ends are indicated by yellow triangles. Scale bars are 1 mm. **(D)** Thin filament lengths from rat neonatal cardiomyocytes expressing GFP, GFP-Lmod2 [WT], and GFP-Lmod2[E34Q]. Representative images and the relationship between sarcomere length and filament lengths are available in Fig. S1, B and C. Each point represents the average measurement per single cell. Mean ± SD, P values are shown on the graph.

same model with a 10-ns step size produced the same correlation while using fewer computational resources. With this approach, we can run simulations and calculate the standard free energy of binding of various Lmod and Tmod point mutations, predict if they increase or decrease complex stability, and then select mutations with desired effects for in vitro and cellular experiments. Consequently, integrating MDS emerges as a promising approach to expedite this process (Kukol, 2014). For a complex formation, using MDS as a first step in predicting the effects of mutations is more time- and effort-efficient than introducing all the mutations, purifying and accurately quantifying proteins, and employing traditional binding assays to study residue-specific interactions. MDS offers the capability to screen multiple mutations and inform us about residue-specific interactions between Lmod2 and Tpm1.1, thereby facilitating the elucidation of key regulatory mechanisms underlying competition between Lmod and Tmod isoforms.

MDS can be applied to other protein complexes to screen for point mutations that induce favorable changes in stability. However, the approach we used is not effective for large structural changes, such as truncations. NMR data on the Lmod2s1/TM1a$_{1-14}$Zip complex indicated that the first 11 residues of Lmod2s1 are dynamic and disordered. By neglecting the temperature entropy product term in the standard Gibbs free energy calculation, our model could not account for the likely effect on entropy that the Δ11 mutation had. This further supports that neglecting the temperature entropy product should only be done when comparing the relative $\Delta G°_{bind}$ of complexes with similar conformational entropy.

In the pyrene-actin polymerization assay used to study the effect of Lmod2 binding on the elongation of preformed actin filaments capped at the barbed end, it was shown that the presence of Tpm1.1 drastically increased the capping ability of Lmod2 (Tsukada et al., 2010). Our second objective was to investigate whether a small change in affinity for Tpm1.1 could

lead to significant alterations in the thin filament length and the localization of Lmod2 and Tmod1 in cardiomyocytes, particularly if the affinity of Lmod2 becomes lower than that of Tmod1. Of several mutations studied, we selected the E34Q mutation for cellular experiments. The E34Q mutation, which modestly affected Lmod2's affinity for Tpm1.1, significantly influenced its competition with Tmod1 in isolated cardiomyocytes. An additional rationale for selecting the E34Q mutation for cellular experiments was that the identical amino acid substitution is present in Lmod3 (Fig. 1 B), and it was not expected to alter the overall Lmod structure or cause significant allosteric changes in other domains. By altering the affinity of Lmod2's Tpm-binding site for Tpm1.1 to become lower than that of Tmod1's Tpm-binding site 1, the ability of Lmod2 to displace Tmod1 from the pointed ends of thin filaments in cardiomyocytes was compromised. Previous studies established that excess WT Lmod2 expression in cardiomyocytes displaced Tmod1 from pointed ends and caused excessive thin filament elongation; the displacement was drastically abrogated in the presence of Lmod2[L25G] (Tolkatchev et al., 2020). Similar to L25G, the hypomorphic E34Q mutation also drastically decreased Lmod2s ability to remove Tmod1 off the pointed end. However, unlike Lmod2[L25G], which completely abolished Lmod2 binding to Tpm1.1, Lmod2[E34Q] showed no visible reduction in localization to pointed ends of thin filaments and was still capable of elongating thin filaments (from 0.75 to 0.83 µm), although not as efficiently as WT Lmod2 (0.87 µm, $P < 0.0001$, Fig. 5 D and Fig. S1, B–D), due to Tmod1's ability to bind and partially block thin filament elongation.

In striated muscle cells, incorporation of rhodamine-labeled actin at the thin filament pointed end was observed, leading to the conclusion that Tmod1 acts as a dynamic cap (Littlefield et al., 2001). This result does not contradict our competition model (Tsukada et al., 2010; Tolkatchev et al., 2022). Lmod2 can temporarily replace Tmod1 at the pointed end, allowing for the addition of new actin monomers.

According to our model of Tmod1 displacement by Lmod2 (Tolkatchev et al., 2022), intrinsically disordered regions of Lmod2 anchor to the pointed end of the thin filament via Tpm-binding site 1 and gradually displace Tmod1 by engaging actin-binding sites one after another. For a polyvalent intrinsically disordered protein, each binding site may bind and unbind relatively independently, as described by Rao et al. (1998). During competitive displacement, there is a stage when both Lmod2 and Tmod1 can be bound on the same thin filament pointed end. For example, when Lmod2 removes Tmod1 from Tpm using Tpm-binding site 1, Tmod1 can still be bound via other sites (e.g., via the Tmod1's Tpm-binding site 2 or its actin-binding sites). If the interaction between Lmod2 and Tpm1.1 weakens, the following steps to complete Tmod1 removal will be prolonged. As a result, we observe both Lmod2 [E34Q] and Tmod1 bound to the same pointed end, although through different interacting sites. Therefore, the results obtained with the expression of Lmod2[E34Q] are consistent with the "stepwise competitive displacement" model. In summary, the data in this study support a model of active competition between Tmod1 and Lmod2 at the pointed ends of thin filaments and underscore the pivotal role of the binding of Tpm-binding site 1 to Tpm1.1 in maintaining the competition balance, which ultimately contributes to determining the length of thin filaments.

Data availability

The datasets generated or analyzed during this study are included in this article and the supplementary data. The raw data are available from the corresponding authors upon reasonable request.

Acknowledgments

Henk L. Granzier served as editor.

The authors would like to thank Christopher Gomez (University of Arizona; UofA) who initiated the cardiomyocyte experiments, Tim Rast (UofA) for cloning the AAV construct, Tania Larrinaga (UofA) for extracting and fixing the cells, Olga Alexhina and the UofA Adenovirus Core for producing the AAV, and Ann Kurain (Mount Sinai) for help with thin filament length measurements. This paper is dedicated to N. Starks, our friend, colleague, and co-author, who passed away on May 8, 2023.

This work was supported by the American Heart Association Grant #826467 to G.E. Smith and by the National Institutes of Health (NIH) R01 GM120137 grant to A.S. Kostyukova and C.C. Gregorio. E. Sánchez Díaz was supported by the Protein Biotechnology Training Program T32 GM008336 at Washington State University. B. Osegueda was supported by the training grants NIH R25 EB027606 and NIH T34GM141971 to Washington State University. S. Novak was supported by R01HL12307801 and C.C. Gregorio was supported by Czarina M. & Humberto S. Lopez Endowed Chair for Excellence in Cardiovascular Research.

Author contributions: E. Sánchez Díaz: formal analysis, investigation, methodology, resources, validation, visualization, and writing—original draft, review, and editing. B. Osegueda: formal analysis, investigation, resources, validation, visualization, and writing—review and editing. S. Minakhina: formal analysis, investigation, validation, visualization, and writing—original draft, review, and editing. N. Starks: investigation, methodology, and resources. S. Novak: investigation, resources, and validation. D. Tolkatchev: methodology and writing—review and editing. C.C. Gregorio: conceptualization, funding acquisition, project administration, resources, supervision, and writing—review and editing. A.S. Kostyukova: conceptualization, funding acquisition, project administration, resources, supervision, validation, and writing—review and editing. G.E. Smith: conceptualization, data curation, formal analysis, investigation, methodology, resources, software, supervision, validation, visualization, and writing—original draft, review, and editing.

Disclosures: The authors declare no competing interests exist.

Submitted: 11 July 2024
Revised: 14 February 2025
Accepted: 30 March 2025

References

Ahrens-Nicklas, R.C., C.T. Pappas, G.P. Farman, R.M. Mayfield, T.M. Larrinaga, L. Medne, A. Ritter, I.D. Krantz, C. Murali, K.Y. Lin, et al. 2019. Disruption of cardiac thin filament assembly arising from a mutation in LMOD2: A novel mechanism of neonatal dilated cardiomyopathy. *Sci. Adv.* 5:eaax2066. https://doi.org/10.1126/sciadv.aax2066

Brown, J.H., and C. Cohen. 2005. Regulation of muscle contraction by tropomyosin and troponin: How structure illuminates function. *Adv. Protein Chem.* 71:121–159. https://doi.org/10.1016/S0065-3233(04)71004-9

Carman, P.J., K.R. Barrie, G. Rebowski, and R. Dominguez. 2023. Structures of the free and capped ends of the actin filament. *Science*. 380:1287–1292. https://doi.org/10.1126/science.adg6812

Case, D.A., H.M. Aktulga, K. Belfon, I.Y. Ben-Shalom, J.T. Berryman, S.R. Brozell, D.S. Cerutti, T.E. Cheatham, G.A. Cisneros, V.W.D. Cruzeiro, et al. 2022. Amber 2022. University of California, San Francisco, CA, USA.

Colpan, M., D. Tolkatchev, S. Grover, G.L. Helms, J.R. Cort, N. Moroz, and A.S. Kostyukova. 2016. Localization of the binding interface between leiomodin-2 and α-tropomyosin. *Biochim. Biophys. Acta*. 1864:523–530. https://doi.org/10.1016/j.bbapap.2016.02.009

Fowler, V.M., and R. Dominguez. 2017. Tropomodulins and leiomodins: Actin pointed end caps and nucleators in muscles. *Biophys. J.* 112:1742–1760. https://doi.org/10.1016/j.bpj.2017.03.034

Freddolino, P.L., S. Park, B. Roux, and K. Schulten. 2009. Force field bias in protein folding simulations. *Biophys. J.* 96:3772–3780. https://doi.org/10.1016/j.bpj.2009.02.033

Gokhin, D.S., and V.M. Fowler. 2017. Software-based measurement of thin filament lengths: An open-source GUI for distributed deconvolution analysis of fluorescence images. *J. Microsc.* 265:11–20. https://doi.org/10.1111/jmi.12456

Greenfield, N.J. 2006. Using circular dichroism collected as a function of temperature to determine the thermodynamics of protein unfolding and binding interactions. *Nat. Protoc.* 1:2527–2535. https://doi.org/10.1038/nprot.2006.204

Greenfield, N.J., and V.M. Fowler. 2002. Tropomyosin requires an intact N-terminal coiled coil to interact with tropomodulin. *Biophys. J.* 82:2580–2591. https://doi.org/10.1016/S0006-3495(02)75600-2

Greenfield, N.J., L. Kotlyanskaya, and S.E. Hitchcock-DeGregori. 2009. Structure of the N terminus of a nonmuscle alpha-tropomyosin in complex with the C terminus: Implications for actin binding. *Biochemistry*. 48:1272–1283. https://doi.org/10.1021/bi801861k

Greenfield, N.J., G.T. Montelione, R.S. Farid, and S.E. Hitchcock-DeGregori. 1998. The structure of the N-terminus of striated muscle alpha-tropomyosin in a chimeric peptide: Nuclear magnetic resonance structure and circular dichroism studies. *Biochemistry*. 37:7834–7843. https://doi.org/10.1021/bi973167m

Gregorio, C.C., A. Weber, M. Bondad, C.R. Pennise, and V.M. Fowler. 1995. Requirement of pointed-end capping by tropomodulin to maintain actin filament length in embryonic chick cardiac myocytes. *Nature*. 377:83–86. https://doi.org/10.1038/377083a0

Gustafson, T.A., J.J. Bahl, B.E. Markham, W.R. Roeske, and E. Morkin. 1987. Hormonal regulation of myosin heavy chain and alpha-actin gene expression in cultured fetal rat heart myocytes. *J. Biol. Chem.* 262:13316–13322. https://doi.org/10.1016/S0021-9258(18)45203-9

Henderson, C.A., C.G. Gomez, S.M. Novak, L. Mi-Mi, and C.C. Gregorio. 2017. Overview of the muscle cytoskeleton. *Compr. Physiol.* 7:891–944. https://doi.org/10.1002/cphy.c160033

Honig, B., and A. Nicholls. 1995. Classical electrostatics in biology and chemistry. *Science*. 268:1144–1149. https://doi.org/10.1126/science.7761829

Hornak, V., R. Abel, A. Okur, B. Strockbine, A. Roitberg, and C. Simmerling. 2006. Comparison of multiple Amber force fields and development of improved protein backbone parameters. *Proteins*. 65:712–725. https://doi.org/10.1002/prot.21123

Izadi, S., R. Anandakrishnan, and A.V. Onufriev. 2014. Building water models: A different approach. *J. Phys. Chem. Lett.* 5:3863–3871. https://doi.org/10.1021/jz501780a

Kollman, P.A., I. Massova, C. Reyes, B. Kuhn, S. Huo, L. Chong, M. Lee, T. Lee, Y. Duan, W. Wang, et al. 2000. Calculating structures and free energies of complex molecules: Combining molecular mechanics and continuum models. *Acc. Chem. Res.* 33:889–897. https://doi.org/10.1021/ar000033j

Kostyukova, A.S. 2007. Leiomodin/tropomyosin interactions are isoform specific. *Arch. Biochem. Biophys.* 465:227–230. https://doi.org/10.1016/j.abb.2007.05.012

Kostyukova, A.S., S.E. Hitchcock-Degregori, and N.J. Greenfield. 2007. Molecular basis of tropomyosin binding to tropomodulin, an actin-capping protein. *J. Mol. Biol.* 372:608–618. https://doi.org/10.1016/j.jmb.2007.05.084

Kukol, A. 2014. Molecular Modeling of Proteins. Humana Press Inc., Totowa, NJ, USA.

Larrinaga, T.M., G.P. Farman, R.M. Mayfield, M. Yuen, R.C. Ahrens-Nicklas, S.T. Cooper, C.T. Pappas, and C.C. Gregorio. 2024. Lmod2 is necessary for effective skeletal muscle contraction. *Sci. Adv.* 10:eadk1890. https://doi.org/10.1126/sciadv.adk1890

Li, N., S. Chen, K. Xu, M.T. He, M.Q. Dong, Q.C. Zhang, and N. Gao 2023. Structural basis of membrane skeleton organization in red blood cells. *Cell*. 186:1912–1929.e18. https://doi.org/10.1016/j.cell.2023.03.017

Li, S., K. Mo, H. Tian, C. Chu, S. Sun, L. Tian, S. Ding, T.R. Li, X. Wu, F. Liu, et al. 2016. Lmod2 piggyBac mutant mice exhibit dilated cardiomyopathy. *Cell Biosci.* 6:38. https://doi.org/10.1186/s13578-016-0101-y

Littlefield, R., A. Almenar-Queralt, and V.M. Fowler. 2001. Actin dynamics at pointed ends regulates thin filament length in striated muscle. *Nat. Cell Biol.* 3:544–551. https://doi.org/10.1038/35078517

Mi-Mi, L., G.P. Farman, R.M. Mayfield, J. Strom, M. Chu, C.T. Pappas, and C.C. Gregorio. 2020. In vivo elongation of thin filaments results in heart failure. *PLoS One*. 15:e0226138. https://doi.org/10.1371/journal.pone.0226138

Nitanai, Y., S. Minakata, K. Maeda, N. Oda, and Y. Maéda. 2007. Crystal structures of tropomyosin: Flexible coiled-coil. *Adv. Exp. Med. Biol.* 592:137–151. https://doi.org/10.1007/978-4-431-38453-3_13

Pappas, C.T., G.P. Farman, R.M. Mayfield, J.P. Konhilas, and C.C. Gregorio. 2018. Cardiac-specific knockout of Lmod2 results in a severe reduction in myofilament force production and rapid cardiac failure. *J. Mol. Cell. Cardiol.* 122:88–97. https://doi.org/10.1016/j.yjmcc.2018.08.009

Pappas, C.T., R.M. Mayfield, C. Henderson, N. Jamilpour, C. Cover, Z. Hernandez, K.R. Hutchinson, M. Chu, K.H. Nam, J.M. Valdez, et al. 2015. Knockout of Lmod2 results in shorter thin filaments followed by dilated cardiomyopathy and juvenile lethality. *Proc. Natl. Acad. Sci. USA*. 112:13573–13578. https://doi.org/10.1073/pnas.1508273112

Pettersen, E.F., T.D. Goddard, C.C. Huang, G.S. Couch, D.M. Greenblatt, E.C. Meng, and T.E. Ferrin. 2004. UCSF Chimera--a visualization system for exploratory research and analysis. *J. Comput. Chem.* 25:1605–1612. https://doi.org/10.1002/jcc.20084

Rao, J., J. Lahiri, L. Isaacs, R.M. Weis, and G.M. Whitesides. 1998. A trivalent system from vancomycin.D-ala-D-Ala with higher affinity than avidin.biotin. *Science*. 280:708–711. https://doi.org/10.1126/science.280.5364.708

Sanner, M.F., A.J. Olson, and J.C. Spehner. 1996. Reduced surface: An efficient way to compute molecular surfaces. *Biopolymers*. 38:305–320. https://doi.org/10.1002/(SICI)1097-0282(199603)38:3<305::AID-BIP4>3.0.CO;2-Y

Schneider, C.A., W.S. Rasband, and K.W. Eliceiri. 2012. NIH image to ImageJ: 25 years of image analysis. *Nat. Methods*. 9:671–675. https://doi.org/10.1038/nmeth.2089

Shabane, P.S., S. Izadi, and A.V. Onufriev. 2019. General purpose water model can improve atomistic simulations of intrinsically disordered proteins. *J. Chem. Theor. Comput.* 15:2620–2634. https://doi.org/10.1021/acs.jctc.8b01123

Sono, R., T.M. Larrinaga, A. Huang, F. Makhlouf, X. Kang, J. Su, R. Lau, V.A. Arboleda, R. Biniwale, G.A. Fishbein, et al. 2023. Whole-exome sequencing identifies homozygote nonsense variants in LMOD2 gene causing infantile dilated cardiomyopathy. *Cells*. 12:1455. https://doi.org/10.3390/cells12111455

Srinivasan, J., T.E. Cheatham, P. Cieplak, P.A. Kollman, and D.A. Case. 1998. Continuum solvent studies of the stability of DNA, RNA, and phosphoramidate - DNA helices. *J. Am. Chem. Soc.* 120:9401–9409. https://doi.org/10.1021/ja981844+

Still, C.W., A. Tempczyk, R.C. Hawley, and T. Hendrickson. 1990. Semianalytical treatment of solvation for molecular mechanics and dynamics. *J. Am. Chem. Soc.* 16:6127–6129. https://doi.org/10.1021/ja00172a038

Sweeney, H.L., and D.W. Hammers. 2018. Muscle Contraction. *Cold Spring Harb. Perspect. Biol.* 10:a023200. https://doi.org/10.1101/cshperspect.a023200

Szikora, S., P. Görög, and J. Mihály. 2022. The mechanisms of thin filament assembly and length regulation in muscles. *Int. J. Mol. Sci.* 23:5306. https://doi.org/10.3390/ijms23105306

Tolkatchev, D., C.C. Gregorio, and A.S. Kostyukova. 2022. The role of leiomodin in actin dynamics: A new road or a secret gate. *FEBS J.* 289:6119–6131. https://doi.org/10.1111/febs.16128

Tolkatchev, D., B. Kuruba, G.E. Smith Jr., K.D. Swain, K.A. Smith, N. Moroz, T.J. Williams, and A.S. Kostyukova. 2021. Structural insights into the tropomodulin assembly at the pointed ends of actin filaments. *Protein Sci.* 30:423–437. https://doi.org/10.1002/pro.4000

Tolkatchev, D., G.E. Smith Jr., and A.S. Kostyukova. 2019. Role of intrinsic disorder in muscle sarcomeres. *Prog. Mol. Biol. Transl. Sci.* 166:311–340. https://doi.org/10.1016/bs.pmbts.2019.03.014

Tolkatchev, D., G.E. Smith Jr., L.E. Schultz, M. Colpan, G.L. Helms, J.R. Cort, C.C. Gregorio, and A.S. Kostyukova. 2020. Leiomodin creates a leaky cap at the pointed end of actin-thin filaments. *PLoS Biol.* 18:e3000848. https://doi.org/10.1371/journal.pbio.3000848

Tsukada, T., C.T. Pappas, N. Moroz, P.B. Antin, A.S. Kostyukova, and C.C. Gregorio. 2010. Leiomodin-2 is an antagonist of tropomodulin-1 at the pointed end of the thin filaments in cardiac muscle. *J. Cell Sci.* 123: 3136–3145. https://doi.org/10.1242/jcs.071837

Uversky, V.N., S.P. Shah, Y. Gritsyna, S.E. Hitchcock-DeGregori, and A.S. Kostyukova. 2011. Systematic analysis of tropomodulin/tropomyosin interactions uncovers fine-tuned binding specificity of intrinsically disordered proteins. *J. Mol. Recognit.* 24:647–655. https://doi.org/10.1002/jmr.1093

Vasilescu, C., M. Colpan, T.H. Ojala, T. Manninen, A. Mutka, K. Ylänen, O. Rahkonen, T. Poutanen, L. Martelius, R. Kumari, et al. 2024. Recessive TMOD1 mutation causes childhood cardiomyopathy. *Commun. Biol.* 7:7. https://doi.org/10.1038/s42003-023-05670-9

Wang, E., H. Sun, J. Wang, Z. Wang, H. Liu, J.Z.H. Zhang, and T. Hou. 2019a. End-point binding free energy calculation with MM/PBSA and MM/GBSA: Strategies and applications in drug design. *Chem. Rev.* 119: 9478–9508. https://doi.org/10.1021/acs.chemrev.9b00055

Wang, E., G. Weng, H. Sun, H. Du, F. Zhu, F. Chen, Z. Wang, and T. Hou. 2019b. Assessing the performance of the MM/PBSA and MM/GBSA methods. 10. Impacts of enhanced sampling and variable dielectric model on protein-protein Interactions. *Phys. Chem. Chem. Phys.* 21: 18958–18969. https://doi.org/10.1039/C9CP04096J

Weber, A., C.R. Pennise, G.G. Babcock, and V.M. Fowler. 1994. Tropomodulin caps the pointed ends of actin filaments. *J. Cell Biol.* 127:1627–1635. https://doi.org/10.1083/jcb.127.6.1627

Winter, J.M., B. Joureau, E.J. Lee, B. Kiss, M. Yuen, V.A. Gupta, C.T. Pappas, C.C. Gregorio, G.J. Stienen, S. Edvardson, et al. 2016. Mutation-specific effects on thin filament length in thin filament myopathy. *Ann. Neurol.* 79:959–969. https://doi.org/10.1002/ana.24654

Yuen, M., S.A. Sandaradura, J.J. Dowling, A.S. Kostyukova, N. Moroz, K.G. Quinlan, V.L. Lehtokari, G. Ravenscroft, E.J. Todd, O. Ceyhan-Birsoy, et al. 2014. Leiomodin-3 dysfunction results in thin filament disorganization and nemaline myopathy. *J. Clin. Invest.* 124:4693–4708. https://doi.org/10.1172/JCI75199

Yuen, M., L. Worgan, J. Iwanski, C.T. Pappas, H. Joshi, J.M. Churko, S. Arbuckle, E.P. Kirk, Y. Zhu, T. Roscioli, et al. 2022. Neonatal-lethal dilated cardiomyopathy due to a homozygous LMOD2 donor splice-site variant. *Eur. J. Hum. Genet.* 30:450–457. https://doi.org/10.1038/s41431-022-01043-8

Supplemental material

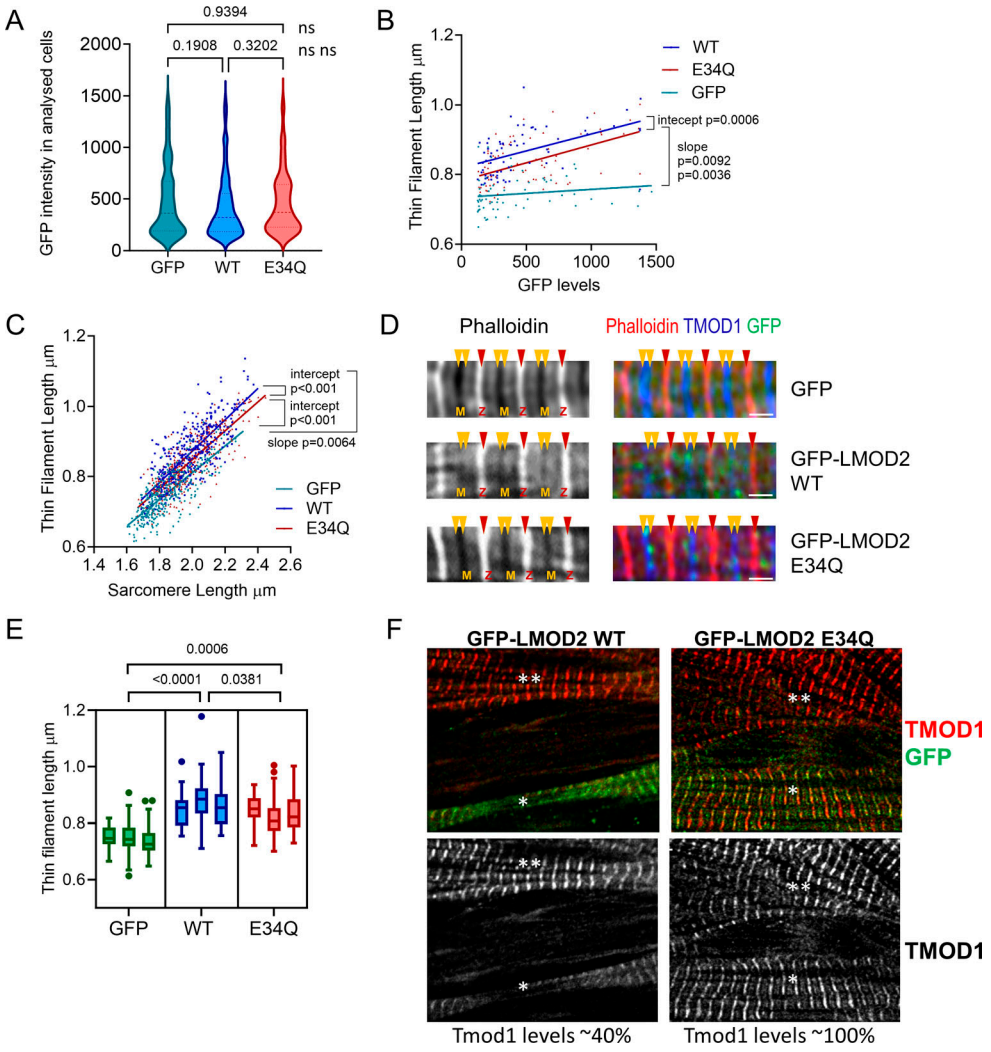

Figure S1. **Analysis of WT and E34Q Lmod2 expression in rat neonatal cardiomyocytes. (A)** Violin plots of average GFP intensities in cardiomyocytes expressing GFP (turquoise), GFP-Lmod2 WT (WT, blue), and GFP-Lmod2 E34Q (E34Q, red), used for Tmod1 and thin filament length assessment (as in Fig. 5). **(B)** Scatter plot showing relationship and variability between levels of GFP-tagged proteins (average GFP intensity per cell, X axis) and thin filament lengths (average per cell, Y axis) in cells expressing GFP (turquoise), GFP-Lmod2 WT (WT, blue), and GFP-Lmod2 E34Q (E34Q, red). Pearson tests show correlation between Lmod2 levels and thin filament length (both WT and E34Q, $P < 0.0001$), but not between GFP alone and thin filament length ($P = 0.219$). The intercepts of GFP-Lmod2 WT and GFP-Lmod2 E34Q significantly differ from each other ($P = 0.0006$), and their slopes differ from GFP alone ($P = 0.0092$, $P = 0.0036$). **(C)** Scatter plot showing relationship between sarcomere (X) and thin filament lengths (Y) in cells expressing GFP (turquoise), GFP-Lmod2 WT (WT, blue), and GFP-Lmod2 E34Q (E34Q, red). The slopes of all three linear regression lines are significantly nonzero ($R^2 = 0.61$, $R^2 = 0.67$, $R^2 = 0.61$, $P < 0.0001$) and significantly different, GFP and WT (slope $P = 0.0064$), GFP and E34Q (intercept $P < 0.0001$), and WT and E34Q (intercept $P < 0.0001$). **(D)** Representative images of relaxed sarcomeres stained for GFP (green), endogenous Tmod1 (blue), and F-actin (phalloidin, red). Yellow arrowheads indicate pointed ends of thin filaments, and red arrowheads show Z-lines. **(E)** Results of nested one-way ANOVA and Tukey multiple comparison tests of three independent thin filament measurement data. **(F)** Comparison of Tmod1 (red) intensities in cells expressing GFP-Lmod2 WT and E34Q (green, marked with *) to the neighboring non-transduced cardiomyocytes (no GFP-Lmod2, marked with**). Example of 60% reduction of Tmod1 levels in GFP-Lmod2 WT cardiomyocytes (left panels) and no change in GFP-Lmod2 E34Q cardiomyocytes (right panels). Scale bars are 1 µm.

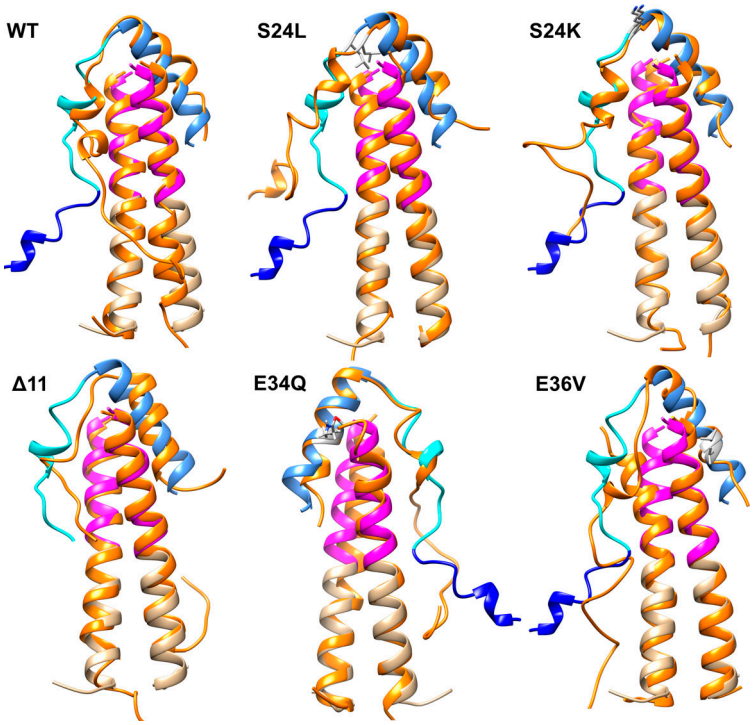

Figure S2. **Alignment of the complex structures obtained after MDS with the complex structures before simulations.** In the original structures, the section in magenta is the first 14 residues of the Tpm1.1 fragment, the section highlighted in tan is the leucine zipper sequence, and the section highlighted in blue is the first 11 residues of the Lmod2 fragment, which were removed in Lmod2s1 Δ11. The section highlighted in cyan represents residues 12–25 of Lmod2s1, and the section highlighted in cornflower blue is the remainder of Lmod2s1 (residues 26–41). The simulated structures are orange. The mutated residues are shown in gray, with side chains displayed for clarity.

Provided online are five tables. Table S1 lists the partially overlapped primers used to introduce mutations. Table S2 shows the $\Delta G°_{bind}$ in (kcal/mole) calculated from MMPB(GB)SA of the 1-µs simulation production run with the 20-ns step interval (total of 50 frames). Table S3 shows the R^2 obtained from a linear fit of the plot of standard free energy of binding from Table S1 versus ΔT_m obtained with a 20-ns step interval. Table S4 shows the R^2 obtained from a linear fit of the plot of standard free energy of binding (MMPBSA triple trajectory) versus ΔT_m obtained with a ε 1 or 2. Table S5 shows the K_d calculated from the unfolding curves.